

Unleashing infinite momentum bandgap using resonant material systems

X. Wang^{1,*}, P. Garg^{2,*}, M. S. Mirmoosa³, A. G. Lampryanidis², C. Rockstuhl^{1,2}, and V. S. Asadchy⁴

¹*Institute of Nanotechnology, Karlsruhe Institute of Technology, Karlsruhe, Germany*

²*Institute of Theoretical Solid State Physics, Karlsruhe Institute of Technology, Karlsruhe, Germany*

³*Department of Physics and Mathematics, University of Eastern Finland, P.O. Box 111, FI-80101 Joensuu, Finland*

⁴*Department of Electronics and Nanoengineering, Aalto University, Espoo, Finland*

The realization of photonic time crystals is a major opportunity but also comes with significant challenges. The most pressing one, potentially, is the requirement for a substantial modulation strength in the material properties to create a noticeable momentum bandgap. Reaching that noticeable bandgap in optics is highly demanding with current, and possibly also future, material platforms since their modulation strength is small by tendency. Here we demonstrate that by introducing temporal variations in a resonant material, the momentum bandgap can be drastically expanded, potentially approaching infinity with modulation strengths in reach with known low-loss materials and realistic laser pump powers. The resonance can emerge from an intrinsic material resonance or a suitably spatially structured material supporting a structural resonance. Our concept is validated for resonant bulk media and optical metasurfaces and paves the way toward the first experimental realizations of photonic time crystals.

INTRODUCTION

Time-varying electromagnetics has emerged as a captivating field of research, capturing significant attention from the scientific community [1, 2]. Within this domain, a recent and intriguing concept that has garnered interest is that of photonic time crystals [3, 4]. Distinct from conventional spatial photonic crystals, photonic time crystals are artificial materials whose electromagnetic properties are uniform in space but periodically modulated in time. This temporal periodicity generates a momentum bandgap in which light exponentially grows over time. Such behavior results in exotic light-matter interaction in the optical regime, including amplification of spontaneous emission of an excited atom [5], subluminal Cherenkov radiation [6], superluminal momentum-gap solitons [7], and others. The momentum bandgap stems from the Bragg-like interference of multiple reflected waves generated at the periodic temporal interfaces, that is, time moments at which the crystal switches its refractive index [1]. To develop a detectable momentum bandgap, the relative change of the refractive index of the crystal $\Delta n/n$ must be comparable to unity [3, 4, 8].

While photonic time crystals have been experimentally confirmed at microwave frequencies [9–11], designing photonic time crystals at optical frequencies remains a prime challenge. Indeed, the material temporal modulation must be extremely fast, typically twice the oscillation period of the light that probes the response. Such a rapid modulation is unreachable with acousto-optic, thermo-optic, or even electro-optic mechanisms which operate up to 100 GHz [12]. All-optical modulation of the refractive index n (e.g., via third-order optical nonlinearities) is currently considered the most prominent approach to realizing photonic time crystals at optical frequencies. However, nonlinear effects in low-loss materials are very

weak, yielding a relative change in the refractive index to saturate at less than 1%. It also implies substantial power densities that can only be achieved through femtosecond laser pulses with low duty cycles (substantially lower than those required for material modulation) [13]. Recently, transparent conductive oxides were suggested as alternative material candidates to synthesize photonic time crystals. In particular, operating at the epsilon-near-zero regime, indium tin oxide (ITO) and aluminium-doped zinc oxide (AZO) were demonstrated to exhibit relative changes in the refractive index of the order of 100% [14–17]. However, they still demand extremely high pumping power densities, i.e., in the order of tens of TW/cm³ [8]. When combined with significant material dissipation, this could lead to rapid thermal damage to the material. Furthermore, the dissipation can lead to the excitation of a parasitic “dynamic-grating” nonlinear effect that may obstruct the observation of the photonic-time-crystal regime [18]. Therefore, only time refraction (single-cycle modulation) has been experimentally realized in transparent conducting oxides to date [19]. Even though the distinction between a photonic time crystal and a parametric amplifier remains challenging, these experiments suggest that photonic time crystals are in reach [20].

To avoid all these obstacles, we introduce a distinct approach to designing photonic time crystals. We capitalize on artificial composites that support high-quality resonances rather than seeking new materials with improved nonlinear characteristics. Interestingly, a similar generic idea was recently suggested in Ref. [21], however, no practical design or implementation was demonstrated. The approach based on resonant artificial composites allows us to create photonic time crystals with pronounced momentum bandgaps with significantly reduced required modulation strength ($\Delta n/n$ ratio) in reach with known

low-loss materials and realistic laser pump powers. We show that at a conceptual level, the resonance can be intrinsic to the material. But we also go beyond and suggest exploiting a resonance sustained by a spatially structured material to significantly lower the requirement on the modulation strength for reaching a notable momentum bandgap. We validate our concept of a resonant photonic time crystal for bulk materials and realistic optical metasurfaces. We show that the momentum bandgap size can be expanded limitlessly under even low modulation strengths (assuming sufficiently small material dissipation). Our results potentially provide the first material platform to realize a photonic time crystal at optical frequencies.

RESULTS

Photonic time crystals made of intrinsically resonant materials

The earlier designs for photonic time crystals relied on varying the density of free-charge carriers in a bulk material, such as the number of electrons per unit volume [14–17]. In this Section, we first demonstrate that this approach is ineffective in achieving a large momentum bandgap. Next, we will show that temporally modulating the material’s resonance frequency significantly increases the bandgap size while having the same modulation strength.

The permittivity of a bulk material with a Lorentzian dispersion whose charge concentration is modulated in time can be written as $\epsilon(\omega, t) = 1 + \omega_p^2(t)/(\omega_{r0}^2 - \omega^2 + j\gamma\omega)$ [22, Sec. 4.3]. Here, $\omega_p(t)$, ω_{r0} , and γ are the plasma frequency, resonance frequency, and the damping factor of the charger carriers in the material, respectively. A time convention as $e^{+j\omega t}$ is considered, with j being the imaginary unit. This form of the complex permittivity function is valid if the damping coefficient and the natural frequency of the material can be assumed to be constant in time [22]. Assuming a time-harmonic modulation of the charge concentration with the magnitude m and modulation frequency ω_m , i.e., $\omega_p^2(t) = \omega_{p0}^2[1 + m \cos(\omega_m t)]$, the permittivity can be written as $\epsilon(\omega, t) = 1 + \chi(\omega)[1 + m \cos(\omega_m t)]$ with $\chi(\omega)$ the stationary dispersive complex susceptibility of the material just considered.

When solving for the eigenmodes to Maxwell’s equations in such a time-varying medium, the temporal modulation induces a split of the degenerate eigenmodes at $\omega = \omega_m/2$, resulting in a momentum bandgap. Assuming a weak modulation strength ($m \ll 1$) [23], the bandgap covers the momentum space from $k = k_-$ to $k = k_+$, where

$$k_{\pm} = \frac{\omega_m}{2c_0} \sqrt{1 + \chi(\omega_m/2)[1 \pm m/2]}. \quad (1)$$

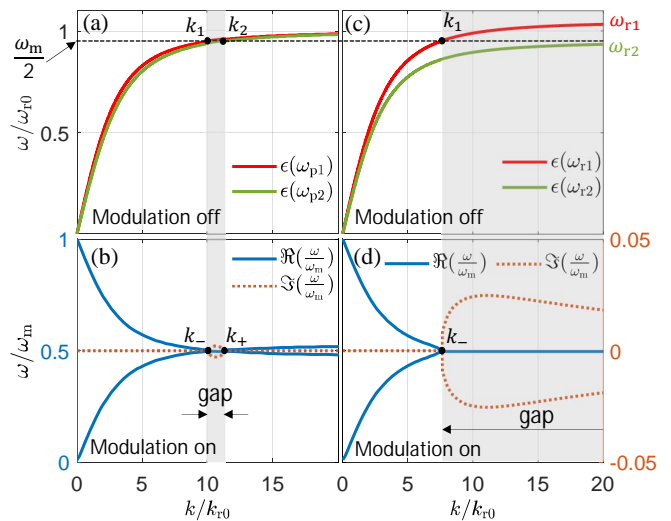


FIG. 1. (a) Dispersion relations of a stationary (not modulated) bulk material when its plasma frequency is $\omega_{p1}^2 = \omega_{p0}^2(1 - m/2)$ (red line) and $\omega_{p2}^2 = \omega_{p0}^2(1 + m/2)$ (green line). (b) Band structure of the time-modulated bulk material when its plasma frequency is modulated as $\omega_p^2(t) = \omega_{p0}^2[1 + m \cos(\omega_m t)]$. The gray region emphasizes the bandgap in (b) and the variation of eigenwavenumber at $\omega = \omega_m/2$ in (a). (c) Dispersion relations of a stationary (not modulated) bulk material when its resonance frequency is $\omega_{r1}^2 = \omega_{r0}^2(1 + m/2)$ (red line) and $\omega_{r2}^2 = \omega_{r0}^2(1 - m/2)$ (green line). (d) Band structure of the time-modulated bulk material when its resonance frequency is modulated as $\omega_r^2(t) = \omega_{r0}^2[1 + m \cos(\omega_m t)]$. In all the subfigures, the wavenumber is normalized by $k_{r0} = \omega_{r0} \sqrt{\epsilon_0 \mu_0}$, and the material parameters are chosen as $m = 0.2$, $\omega_m/2 = 0.95\omega_{r0}$, $\gamma = 0$, and $\omega_{p0} = 3.5\omega_{r0}$.

The detailed derivation of (1) can be found in Sec. 1 of the Supplementary Material [24]. Here, c_0 is the speed of light in a vacuum, and $\gamma = 0$ was assumed. We plot the dispersion relation in the first Brillouin zone of such a photonic time crystal in Fig. 1(b), taking as an example $m = 0.2$ (other material parameters are specified in the figure caption). Inside the momentum bandgap, the eigenfrequency has two complex solutions with positive and negative imaginary parts corresponding to the exponentially decaying and growing modes in time (dashed orange lines).

The weak-modulation approximation is very powerful. Not only does it allow us to find a closed-form solution for the edges of the momentum bandgap, but it also highlights a crucial observation. As is seen from Eq. (1), the bandgap edges k_- and k_+ in the modulated material precisely correspond to the eigenwavenumbers k_1 and k_2 of two non-modulated (stationary) materials with scaled susceptibilities $\chi(\omega)(1 \pm m/2)$ evaluated at the frequency $\omega = \omega_m/2$. Indeed, inside a stationary material, the eigenwavenumber is given by $k(\omega) = \omega \sqrt{1 + \chi(\omega)}/c_0$. This correspondence is rather general and applies to all the photonic time crystal topologies with $m \ll 1$ explored

in this work, including the case when the material is lossy. Interestingly, even when the modulation strength becomes large, the correspondence has only a small error (less than 2% and 5% for $m = 0.5$ and $m = 0.9$, respectively).

Figure 1(a) depicts the dispersion relations of the two stationary materials with scaled susceptibilities. Since χ is linearly proportional to ω_p^2 , the two materials can be alternatively described with scaled plasma frequencies $\omega_{p1}^2 = \omega_{p0}^2(1 - m/2)$ and $\omega_{p2}^2 = \omega_{p0}^2(1 + m/2)$. Thus, by plotting the dispersion relation of the material with modulation turned off, one can determine the momentum bandgap size for a given modulation. We emphasize this property in Figs. 1(a) and (b) using a vertically shaded region. More importantly, this correspondence provides a simple visual insight into how a given material dispersion affects the bandgap size and position. It is clear from Fig. 1(a) that the temporal modulation of the plasma frequency results in a relatively narrow bandgap. The narrow bandgap is caused by the tiny variation of the dispersion curves of a stationary material when the resonance frequency is fixed ($k_1 \approx k_2$). The relative size of the obtained bandgap, calculated as the gap-to-midgap ratio $\Delta k = 2|(k_2 - k_1)/(k_1 + k_2)|$, reaches only 10.3%.

On the contrary, when the resonance frequency ω_r is time-modulated while the plasma frequency ω_p and damping factor γ are fixed, the momentum bandgap can be qualitatively different. Now, we assume that the intrinsic resonance frequency is modulated harmonically so that $\omega_r^2(t) = \omega_{r0}^2[1 + m \cos(\omega_m t)]$. Following the above-described correspondence between the stationary and modulated material scenarios for $m \ll 1$, we plot in Fig. 1(c) the dispersion relation of a stationary bulk material for two values of the resonance frequency: $\omega_{r1}^2 = \omega_{r0}^2(1 + m/2)$ and $\omega_{r2}^2 = \omega_{r0}^2(1 - m/2)$. All other material properties remain the same and are mentioned in the figure caption. It is evident that for the same value of $m = 0.2$, the two dispersion curves now differ significantly at $\omega = \omega_m/2$. When choosing $\omega_{r2} < \omega_m/2 < \omega_{r1}$, the horizontal dashed line at $\omega = \omega_m/2$ intersects only with one of the dispersion curves, at $k = k_1$ (Fig. 1(c)). This indicates that the momentum bandgap in the corresponding time-modulated material has only one edge and extends infinitely towards higher momenta, as shown by the gray-shaded region in the figure. Indeed, by rigorously computing the band structure for this scenario, we observe a semi-infinite momentum bandgap whose edge at k_- is located right at k_1 for the corresponding stationary material (see Fig. 1(d)). The detailed derivations for the band structure extraction can be found in Sec. 2 of the Supplementary Material [24]. The imaginary part of the eigenfrequency inside the bandgap is significantly increased compared to modulating the plasma frequency. Moreover, the shape of the imaginary part curve (orange dashed line) is not typical. It points out that waves with different momentum k can have different and, in princi-

ple, engineered amplification rates. We observed that by changing ω_m within the range $\omega_{r2} < \omega_m/2 < \omega_{r1}$, it is possible to control the curve shape.

Since, in realistic scenarios, near the resonance, material losses tend to increase, it is crucial to explore how a nonzero damping factor γ influences the band structure. The effect of losses is studied in Sec. 3 of the Supplementary Material [24]. In the presence of loss, the imaginary parts of eigenfrequencies exhibit a positive offset, resulting in reduced temporal amplification rates. In contrast, the bandgap size remains. Even when considering losses, the amplification rate remains significantly higher compared to modulating the plasma frequency in the lossless case.

The temporal modulation of the intrinsic resonance frequency of a bulk material can be achieved, for example, through strong dynamic electric biasing [25] but, in practice, could be very challenging. Figure 2(a) illustrates this scenario where an external electric field modulates the effective spring constants κ of each nucleus-electron oscillator. However, instead of modulating materials by modulating the intrinsic resonance frequency of their natural atoms, we propose exploiting a metamaterial concept and utilizing the resonances in metamaterials generated through spatially structured meta-atoms. A conceptual illustration of our proposal is depicted in Fig. 2(b). The metamaterial consists of meta-atoms (with spherical shapes as an example) whose material properties (permittivity ϵ_r or permeability μ_r), radius, or mutual separation distance can be modulated in time. Each of these modulation mechanisms leads to the modulation of the effective resonance frequency $\omega_r^{\text{eff}}(t)$ of the metamaterial. Probably, the most practical scenario is when the plasma frequency of the meta-atom's material is modulated, which can be achieved with the current optical modulation techniques [14–17].

In what follows, instead of relying on bulk metamaterial geometries, we exploit the recently proposed idea of constructing photonic time crystals using metasurfaces [11]. First, we explore the concept by designing resonant metasurfaces using a generic LC-model applicable to all operating frequencies. Then, we provide a feasible optical example of the photonic time crystal – a two-dimensional array of spherical particles – supporting a large momentum bandgap at realistic pump energies.

Photonic time crystals based on resonant metasurfaces

We consider the photonic time crystal in a metasurface geometry. The metasurface is assumed to support surface waves bound to the xy -plane, see Fig. 3(a). The meta-atoms are deeply sub-wavelength and are all equivalent, resulting in a spatial homogeneity of the metasurface at $z = 0$. Similarly to how bulk photonic time crystals

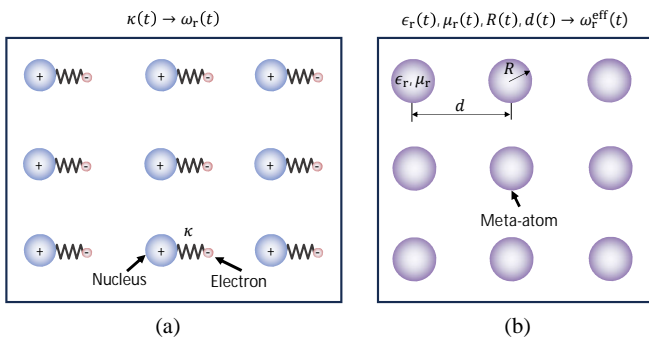


FIG. 2. (a) Illustration of the temporal modulation of the intrinsic resonance frequency of a bulk material. The modulation can be described by a time-varying effective spring constant $\kappa(t)$. (b) Illustration of the temporal modulation of the resonance frequency of a metamaterial consisting of meta-atoms. The modulation can be achieved in various ways, including modulating the permittivity ϵ_r or permeability μ_r of the material from which the meta-atoms are made, the size of the meta-atoms R , or the metamaterial periodicity d .

exhibit momentum bandgaps Δk for bulk propagating eigenmodes, the metasurface-based counterparts support momentum bandgaps Δk_{\parallel} for surface and/or propagating eigenmodes [11] (k_{\parallel} denotes the parallel component of the wavenumber). While here we model the metasurface as an impenetrable impedance boundary, the same qualitative results hold true for penetrable metasurfaces (see the next Section). A resonant impenetrable metasurface can be described by effective reactive parameters, the surface capacitance C and the surface inductance L connected in parallel (Fig. 3(a)). The advantage of this generic LC -model is its ability to describe the interaction of light with a time-modulated metasurface without restricting ourselves to any specific geometry and operational frequency band. At optical frequencies, as we show in the following section, such a resonant metasurface can be made from a two-dimensional array of spherical particles with a time-modulated dielectric constant. At microwave frequencies, the implementation could be based on a mushroom-type high-impedance surface with varactors embedded between adjacent patches [11, 26].

In our model, the surface capacitance is modulated in time harmonically as $C(t) = C_0[1 + m \cos(\omega_m t)]$, while the surface inductance L remains constant. Here, C_0 is the time-averaged value of the capacitance. Such a configuration effectively provides the temporal modulation of the resonance frequency. Without loss of generality, we consider a transverse-magnetic (TM) polarization of the surface waves. Similarly to the derivation in the previous Section, we solve for the eigenmodes of the time-modulated metasurface (see Sec. 4 of the Supplementary Material [24]). Using the weak-modulation approximation ($m \ll 1$), the edges of the momentum bandgap at

$\omega = \omega_m/2$ can be calculated as

$$k_{\parallel}^{\pm} = \frac{\omega_m}{2c_0} \sqrt{1 - \frac{Y_0^2}{Y_{\pm}^2}}, \quad (2)$$

where $Y_0 = \sqrt{\epsilon_0/\mu_0}$ is the free-space wave admittance and $Y_{\pm} = j\frac{\omega_m}{2}C_0(1 \pm \frac{m}{2}) + \frac{1}{j\frac{\omega_m}{2}L}$. In agreement with our findings in the previous Section, the expressions for the edges of the momentum bandgap k_{\parallel}^+ and k_{\parallel}^- precisely correspond to the eigenwavenumbers $k_{\parallel,1}$ and $k_{\parallel,2}$ of two non-modulated impedance surfaces with scaled surface capacitances $C_1 = C_0(1 + \frac{m}{2})$ and $C_2 = C_0(1 - \frac{m}{2})$ evaluated at the frequency $\omega = \omega_m/2$. This is clearly seen from the dispersion relation of an impedance boundary $k_{\parallel}(\omega) = \frac{\omega}{c_0} \sqrt{1 - Y_0^2/Y(\omega)}$ [27, p. 234], where $Y(\omega) = j\omega C + 1/j\omega L$ is the admittance of the parallel connection of the capacitance C and inductance L .

It should be noted that Eq. (2) holds true only for frequencies $\omega_m/2 < 1/\sqrt{LC_0(1 + m/2)} = \omega_{r1}$ (see Sec. 4 of Supplementary Material [24] for more details). At the critical frequency of $\omega_m/2 = \omega_{r1}$, the denominator in Eq. (2) approaches zero, which results in the semi-infinite bandgap ($Y_+ \rightarrow j0$ and, therefore, $k_{\parallel}^+ \rightarrow +\infty$). By working in the regime where $\omega_{r1} < \omega_m/2 < \omega_{r2}$, we can ensure that the momentum bandgap is semi-infinite (here, $\omega_{r2} = 1/\sqrt{LC_0(1 - m/2)}$). For larger modulation frequencies, the bandgap becomes closed. In Fig. 3(b), we plot a band diagram for a time-modulated impedance surface for the case of $m = 0.2$ and $\omega_m/2 = \omega_{r0} = 1/\sqrt{LC_0}$ (lower panel) together with the corresponding dispersion relations for stationary surfaces (upper panel). As expected, the bandgap size can be determined by the two dispersion curves of stationary surfaces with $C_1 = 1.1C_0$ and $C_2 = 0.9C_0$, in particular, by the points where they cross with the horizontal dashed line at ω_{r0} . As is seen, the bandgap size extends from $k_{\parallel} \approx 4k_{r0}$ ($k_{r0} = \omega_{r0}/c_0$) to infinity.

Next, we verify with full-wave simulations (see Methods) the wave evolution inside the momentum bandgap. A stationary capacitive surface is excited from the left by a surface wave with momentum $k_{\parallel} = 5k_{r0}$ (see Fig. 3(c)). From the time moment $t = 0$, the surface capacitance is harmonically modulated in time, resulting in the exponential growth of the surface mode and the higher-order frequency harmonics (some of them being inside the light cone are propagating). This growth is seen in the magnetic-field snapshot taken at $t = 30T_m$ ($T_m = 2\pi/\omega_m$) depicted in the lower panel of Fig. 3(c). Due to the temporal modulation, the momentum of the eigenwaves remains unchanged. However, the modulation generates backward and forward harmonics with equal amplitudes, resulting in a standing wave along the horizontal direction [11]. The complete field evolution animation is available in movie S1. For comparison, we also analyze the case when the boundary is excited by a surface wave with

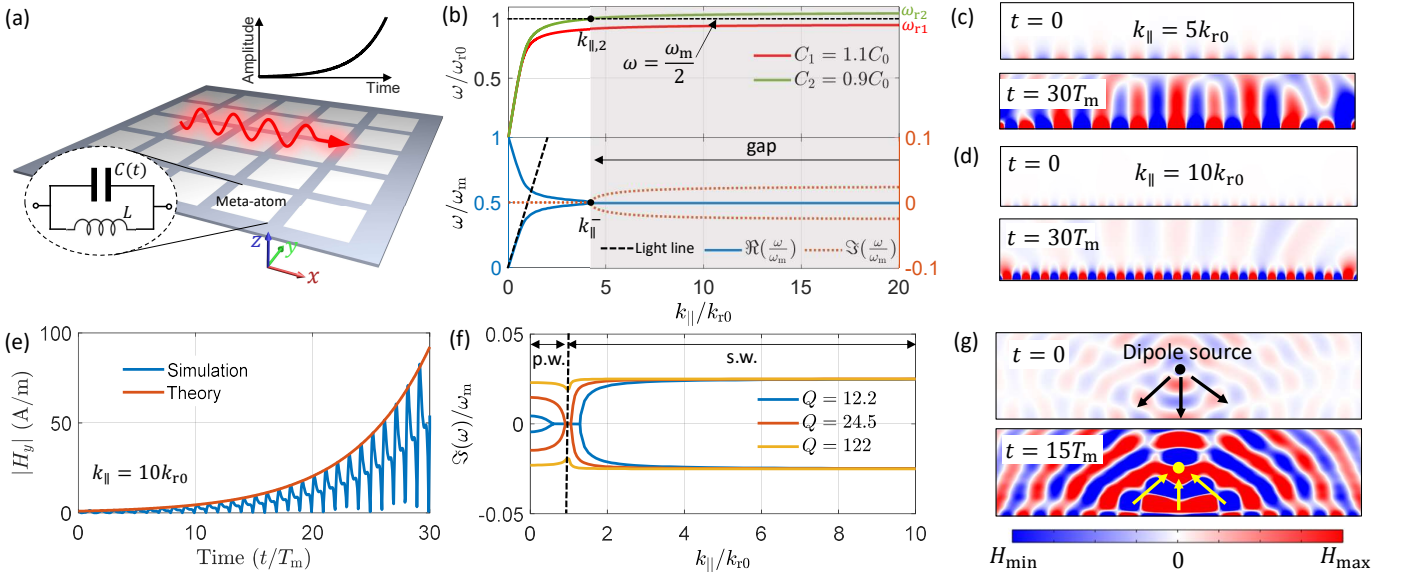


FIG. 3. (a) Generic illustration of a time-varying resonant LC metasurface. Each meta-atom is described by a time-modulated surface capacitance $C(t)$ and a constant surface inductance L . The red arrow indicates a surface eigenmode whose amplitude is growing in time due to its wavenumber being inside the momentum bandgap of the metasurface. (b) Upper: Dispersion relations of a stationary metasurface for the two scaled values of the surface capacitance. Lower: Band structure of the time-modulated resonant metasurface with $C(t) = C_0[1 + m \cos(\omega_m t)]$. The gray region emphasizes the bandgap in the lower panel and the variation of eigenwavenumber at $\omega = \omega_m/2$ in the upper panel. (c) and (d) magnetic field snapshots for momenta $\beta = 5k_{r0}$ and $\beta = 10k_{r0}$ above the metasurface at the time moment when modulation switches on ($t = 0$) and after some time passed ($t = 30T_m$). (e) Time evolution of the magnetic field above the metasurface ($z = 0$) calculated with full-wave simulations and analytically from the band structure. The theoretical amplitude is calculated as $H_y(t) = H_{y0} \exp[\Im(\omega)t]$ where $H_{y0} = 1$ A/m is the initial field at $t = 0$ and $\Im(\omega) = 0.025\omega_m$. (f) Imaginary part of the eigenfrequency for metasurfaces with different quality factors. The real part of eigenfrequency is fixed as $\Re(\omega) = \omega_m/2$. The black dashed line separates propagating waves (p.w.) and surface waves (s.w.). (g) The magnetic field evolution for a dipole source positioned above the time-varying LC metasurface. Due to the infinite bandgap, all momenta $k_{||}$ are amplified by the metasurface. In all the subfigures, $m = 0.2$ was chosen. In Figs. 3(c)(d)(g), the excitation source is turned off after modulation starts.

wavenumber $k_{||} = 10k_{r0}$ (Fig. 3(d)). This wave experiences an even faster exponential growth since the imaginary part of the frequency $\Im(\omega)$ inside the bandgap is larger in this case (see the lower panel of Fig. 3(b)). In Fig. 3(e), we plot the simulated magnetic-field evolution in time (blue curve) for the latter case. The exponential growth of the field amplitude in time coincides with the rate predicted by the theory.

It is important to analyze how the momentum bandgap of the modulated metasurface depends on its quality factor. For that, we reduce the inductance and increase the capacitance at the same rate to preserve the resonance frequency of the stationary metasurface. The quality factor of the stationary metasurface can be qualitatively described as a quality factor of an RLC circuit (where $R = \sqrt{\mu_0/\epsilon_0}$ is the free-space characteristic impedance which is connected in parallel to the metasurface equivalent circuit), that is, $Q = \omega_{r0}C_0\sqrt{\mu_0/\epsilon_0}$ [28, Sec. 6.1]. For each real value of $k_{||}$, we fix $\Re(\omega) = \omega_m/2$ and calculate for the imaginary part of the frequency $\Im(\omega)$ that indicates the presence or absence of the bandgap. Figure 3(f) plots $\Im(\omega)$ for three metasurfaces with differ-

ent quality factors. One can see that metasurfaces with a higher Q -factor provide wider momentum bandgaps for surface waves (s.w.) with larger amplification rates assuming the same modulation function. In comparison, the metasurface for which the results are shown in Figs. 3(b)–(e) has $Q = 2.44$. Moreover, for sufficiently large Q -factors ($Q \geq 9.75$), a second momentum bandgap opens inside the light cone, i.e., for propagating waves (p.w.). Such a regime of the open bandgap for propagating modes is inherent to metasurfaces with high quality factors and cannot occur in non-resonant metasurfaces like those in Ref. [11]. The size of the second bandgap grows with the quality factor of the metasurface since resonances with longer lifetimes suffer from smaller radiation loss and need a weaker modulation to maintain the same amplification rate. It should be noted that the amplification of surface and oblique propagating waves in the metasurface is independent of the phase of the incident light in sharp contrast to conventional parametric degenerate amplifiers [11].

When the quality factor takes sufficiently large values, the two bandgaps merge, and the metasurface can am-

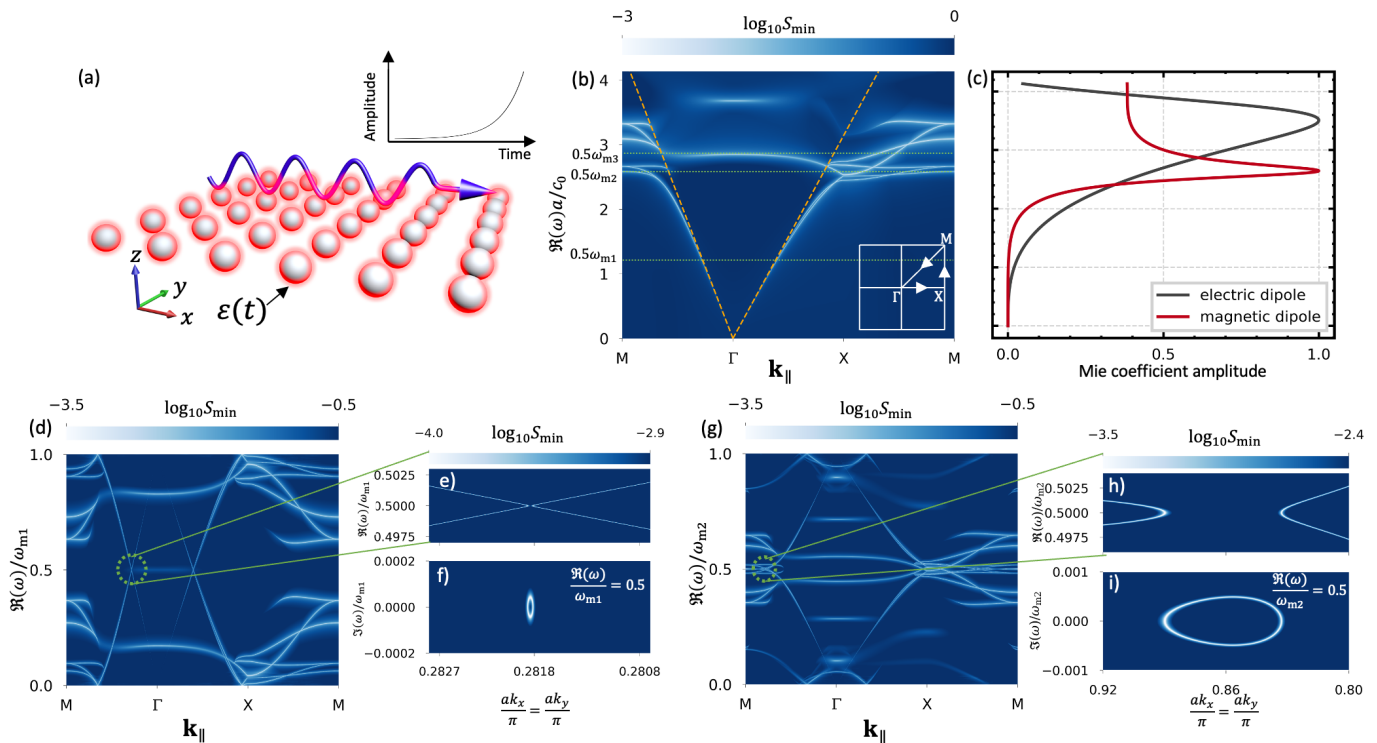


FIG. 4. (a) A representative design of a photonic time crystal based on an optical time-varying resonant metasurface made of dielectric spheres. The purple arrow indicates a surface eigenmode whose amplitude grows in time due to its wavenumber being inside the momentum bandgap of the metasurface. (b) Band structure of a time-invariant metasurface. The color denotes the lowest singular value S_{\min} of the matrix in Eq. (5). The orange dotted lines represent the light lines. (c) The two lowest-order Mie coefficients of an isolated time-invariant sphere. The vertical scale is the same as in (b). (d) Band structure of a time-varying metasurface with modulation frequency ω_{m1} (non-resonant case). (e) Zoomed band structure in the green highlighted region of (d). (f) The corresponding imaginary part of the frequency for fixed $\Re(\omega) = \omega_{m1}/2$. (g)–(i) Original and zoomed band structures of a time-varying metasurface with modulation frequency ω_{m2} (resonant case).

ply incident waves with all possible momenta k_{\parallel} (see the curve for $Q = 122$ in Fig. 3(f)). To demonstrate this infinite momentum bandgap, we place a dipole emitter above the metasurface (Fig. 3(g)). The dipole radiation includes a wide spectrum of momenta, as shown in the upper panel of the figure. Once the temporal modulation of the metasurface is on, waves with all different momenta are amplified and radiated in the specular and retro-directions with respect to the source, see the lower panel in Fig. 3(g). This leads to interesting possibilities such as amplified emission and lasing of light from a radiation source [5]. In contrast to the idea suggested in [5], due to the infinite bandgap, here it is possible to amplify emission with a large and, in principle, tunable spectrum of wavenumbers. This provides opportunities for beam shaping of the amplified signal and for creating perfect lenses (evanescent content of the source radiation can be reconstructed effectively [29] thanks to the amplification of all k_{\parallel}).

Optical implementation

To provide a feasible optical realization of the resonant photonic time crystal, we consider a penetrable metasurface consisting of dielectric spheres with a time-varying permittivity (see Fig. 4(a)). For simplicity, we consider the metasurface being surrounded by air. Here, each sphere effectively behaves as an LC resonator as it supports Mie resonances [30]. The spheres are arranged in an infinite square lattice with the period a . The radius of each sphere is R . For simplicity, we ignore material dispersion. As we verified numerically, it does not significantly modify the bandgap width. Therefore, the permittivity of each sphere reads $\varepsilon(t) = 1 + \chi_0[1 + m\cos(\omega_m t)]$ [22, Sec. 4.3]. Varying the permittivity in time effectively modulates the Mie resonance frequencies of the spheres (see Fig. 2(b)). Such a metasurface corresponds to a (2+1)-dimensional spatiotemporal crystal. In the following, we rely on the T-matrix method to study the optical response from such a metasurface [31] (see Sec. 5 of the Supplementary Material [24] for more details). Furthermore, the calculation

method for band structures using the T-matrix method has been described in the Materials and Methods Section. Hereafter, the radius of the spheres R is fixed at 810 nm, and the lattice period a is set to $3R$. The material susceptibility is chosen $\chi_0 = 10.68$, corresponding to silicon which is nearly lossless and dispersionless in the considered infrared frequency regime.

First, using Eq. (5), we calculate the band structure of a time-invariant metasurface substituting $m = 0$ and $\omega_m = 0$ (Fig. 4(b)). One can see flat bands that occur near the M and X points of the spatial Brillouin zone due to the Mie resonances of the single sphere. For comparison, we plot the absolute values of the dipolar Mie coefficients of a time-invariant single sphere in Fig. 4(c) [30]. From Fig. 4(c), we observe the occurrence of a magnetic dipolar and an electric dipolar resonance that explain the existence of flat bands in Fig. 4(b). As will be shown below, exploiting these resonances dramatically reduces the modulation strength m for attaining wide momentum bandgaps. Note that the band structure shown hereafter accommodates the eigenmodes for both TM and transverse electric (TE) polarizations, however, in what follows, we optimize the metasurfaces for TE-waves.

Next, we plot the band structures of time-varying metasurfaces. We start by choosing the modulation frequency to be $\omega_{m1} = 300$ THz as shown in Fig. 4(b). Since $\frac{\omega_{m1}}{2}$ is away from the flat bands, this configuration corresponds to a scenario of modulating a non-resonant metasurface. Moreover, we observe that the dispersion around $\omega = \frac{\omega_{m1}}{2}$ is linear [see Fig. 4(b)]. This is because the metasurface is spatially homogenizable near and below $\omega = \frac{\omega_{m1}}{2}$ [32]. Therefore, the time-varying metasurface with ω_{m1} mimics the properties of a conventional (space-uniform) photonic time crystal with the modulated plasma frequency. In Fig. 4(d), we show the band structure of this nonresonant metasurface. We choose $m = 0.01$ that corresponds to the relative change of the refractive index $\Delta n/n \approx m\chi_0/(1 + \chi_0) = 1\%$, which is the maximum attainable value for the nonlinear effects in low-loss materials with realistic pump powers [8]. We observe the folding of the band structure of the time-invariant case [3, 33]. At the band crossing in the $\Gamma - M$ region, the momentum bandgap appears, as is seen in the zoomed region (Fig. 4(e)). For plotting the band structures, we limit ourselves only to the dominant dipolar moments in the vector spherical expansion and to the three dominant frequency harmonics (see Sec. 5 in Supplementary Material [24]). While this assumption does not modify the response of the metasurface inside the momentum bandgap, it allows to eliminate side-bands in the band structure. The calculated relative gap width is very narrow, $\Delta k_{\parallel} = 0.0183\%$. We also plot the imaginary part of the frequency $\Im(\omega)$ for a fixed $\Re(\omega) = \frac{\omega_{m1}}{2}$ (see Fig. 4(f)). As expected, in the middle of the bandgap, $\Im(\omega)$ reaches the largest absolute value. Since the bandgap lies below the light cone [see

Fig. 4(b)], only surface-wave incident excitations couple to the modes inside it.

In sharp contrast to the previous case, when half of the modulation frequency is at the position of the magnetic Mie resonance of the spheres (see the horizontal line $0.5\omega_{m2} = 317$ THz in Fig. 4(b)), the bandgap greatly expands. Keeping for a fair comparison the same modulation strength $m = 0.01$, the relative bandgap size of this resonant metasurface reaches the value of $\Delta k_{\parallel} = 6.59\%$, as is calculated from the band structure in Figs. 4(g)–(i). Remarkably, the resonance of the metasurface leads to the widening of the bandgap by a factor of about 350 as compared to the non-resonant case. It should be noted that the correspondence between a time-varying system and two stationary systems with scaled parameters also holds for this metasurface (see Sec. 7 in the Supplementary Material [24]). It is essential to note from Figs. 4(g) that the momentum bandgap is not complete since there exist bands at the $\Re(\omega) > \omega_{m2}/2$ within the bandgap. Nevertheless, in contrast to spatial photonic crystals with their energy bandgaps, the modes inside an incomplete momentum bandgap are always dominant due to their amplifying nature [4]. The comparison of Figs. 4(f) and (i) reveals that the structural resonance not just enhances the bandgap size, but the amplification rate also greatly increases: $\Im(\omega)$ is an order of magnitude larger for the resonant case.

While in the above-considered scenarios, the bandgaps occurred below the light cone, we designed as next a metasurface to generate bandgaps for propagating waves (see illustration in Fig. 5(a)). From Fig. 4(b) for a stationary metasurface, we observe the existence of a flat band within the light cone at the spectral location $\omega = \omega_{m3}/2 = 351$ THz around the Γ -point. Note that because the modes in the flat band lie within the light cone, they correspond to a leaky zone in the band structure. In literature, such modes are termed as guided resonances [34]. By modulating the metasurface periodically at the modulation frequency ω_{m3} , we obtain the band structure shown in Fig. 5(b) ($m = 0.06$ in this case). The zoomed region of the band structure with the momentum bandgap is plotted in Figs. 5(c)–(d). Remarkably, despite the small modulation strength, the momentum bandgap is very large and spans over a wide range of incident angles: up to 54° in the incidence plane parallel to $\Gamma - M$ and 33° parallel to $\Gamma - X$. Due to the almost constant $\Im(\omega)$ inside the bandgap (Fig. 5(d)), the waves that couple to the eigenmodes in the bandgap get amplified at nearly the same rates irrespective of the value of \mathbf{k}_{\parallel} . Importantly, as mentioned in the previous Section, the bandgap for propagating waves is unique to resonant metasurfaces and does not occur for continuous material slabs. We explain the fact that the bandgap in Fig. 5(b) does not span all possible \mathbf{k}_{\parallel} due to relatively low quality factor of magnetic Mie resonances in the spheres as predicted in the LC circuit analysis and limited value of

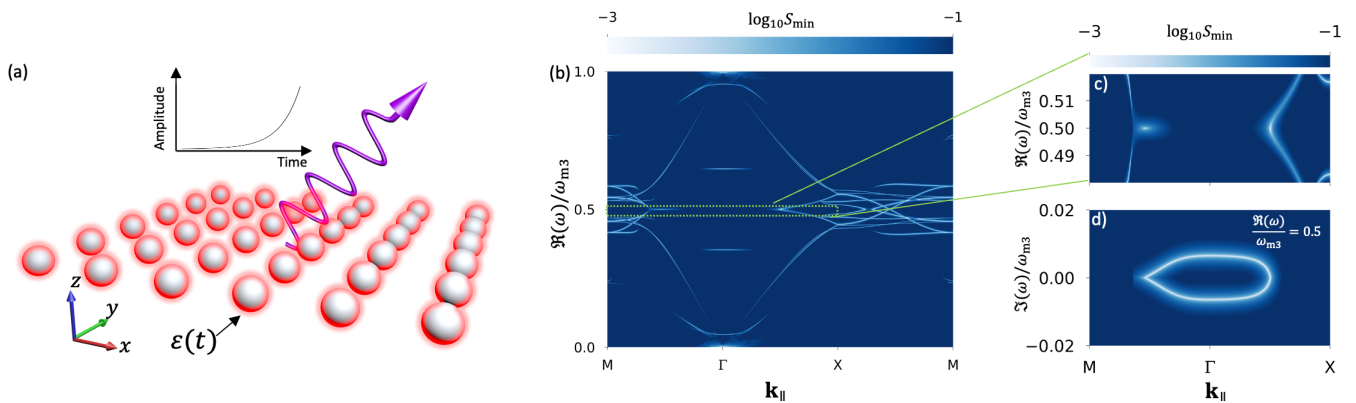


FIG. 5. (a) Optical time-varying metasurface designed to exhibit a momentum bandgap for propagating waves. The purple arrow indicates a propagating eigenmode whose amplitude is growing in time. The geometry of the metasurface is the same as in Fig. 4(a). (b) Band structure of a time-varying metasurface with modulation frequency ω_{m3} . (c) Zoomed band structure in the green highlighted region in (b). (d) The corresponding imaginary part of the frequency for fixed $\Re(\omega) = \omega_{m3}/2$.

m . We foresee that the infinite-bandgap regime as in Figs. 3(f)–(g) can be achieved in the optical metasurface by tuning $\omega_m/2$ to the frequency of the higher-order Mie resonances of the spheres.

DISCUSSION

The pivotal challenge in realizing photonic time crystals in the optical domain lies in generating a substantial and detectable momentum bandgap under current modulation limitations. In this work, we introduce a novel and pragmatic platform based on structured materials to overcome this problem, achieving a significant momentum bandgap under realistic pump conditions. In particular, our findings underscore that by exploiting structural resonances in material, we can achieve a great enhancement of the momentum bandgap size (350 times wider compared with the same material without spatial structuring) with the modulation strength as small as 1%. In principle, a strong resonance has the potential to extend the momentum bandgap infinitely. A distinctive feature of our approach is that the achieved momentum bandgap can cover the entire k -space, encompassing both free-space propagating modes and surface modes. This fundamentally provides new physics compared to the implementations based on bulk media [4, 8] that only support propagating modes and non-resonant metasurfaces [11] that operate exclusively with surface modes. From this point of view, our approach holds novel opportunities for designing more complex photonic time and space-time crystals as well as for amplifying the spontaneous emission of light from emitters located near the structure. Moreover, the designed crystal could be useful for designing a perfect lens, a long-standing goal in optics, since the information of an object carried by evanescent modes can be effectively amplified, resulting

in a highly-resolved image of the object. While our example metasurface operates in the infrared spectrum, it can be extended to the visible spectrum with other materials. In addition, the shape of the meta-atoms is not restricted to spherical, and they can be deployed over a substrate. We anticipate and encourage experimental endeavors to facilitate the proposed approach.

MATERIALS AND METHODS

Calculation of eigenmodes of a metasurface with time-varying spheres

Eigenmodes of a scattering structure are self-standing modes that exist without incident excitation. We use the T-matrix method to evaluate the eigenmodes of the time-varying metasurface. For details on the method, see Sec. 5 in Supplementary Material [24]. Combining Eqs.(S29) and (S30), we write

$$\mathbf{A}^{\text{sca}} = \left(\hat{\mathbf{U}} - \hat{\mathbf{T}}^{(s)}(\omega) \cdot \sum_{\mathbf{R}' \neq 0} \hat{\mathbf{C}}^{(3)}(-\mathbf{R}') e^{-j\mathbf{k}_{\parallel} \cdot \mathbf{R}'} \right)^{-1} \cdot \hat{\mathbf{T}}^{(s)}(\omega) \cdot \mathbf{A}^{\text{inc}}. \quad (3)$$

Next, we use $\mathbf{A}^{\text{inc}} = 0$ in Eq. (3). Therefore, we can rewrite Eq. (3) as

$$\left(\hat{\mathbf{U}} - \hat{\mathbf{T}}^{(s)}(\omega) \cdot \sum_{\mathbf{R}' \neq 0} \hat{\mathbf{C}}^{(3)}(-\mathbf{R}') e^{-j\mathbf{k}_{\parallel} \cdot \mathbf{R}'} \right) \cdot \mathbf{A}^{\text{sca}} = 0. \quad (4)$$

Finally, for Eq. (4) to have a non-trivial solution i.e., $\mathbf{A}^{\text{sca}} \neq 0$, we arrive at the condition

$$\left| \hat{\mathbf{U}} - \hat{\mathbf{T}}^{(s)}(\omega) \cdot \sum_{\mathbf{R}' \neq \mathbf{0}} \hat{\mathbf{C}}^{(3)}(-\mathbf{R}') e^{-j\mathbf{k}_{\parallel} \cdot \mathbf{R}'} \right| = 0. \quad (5)$$

Here, the values of ω and \mathbf{k}_{\parallel} for which Eq. (5) is satisfied correspond to the location of the eigenmodes of the time-varying metasurface. Note that instead of calculating the determinant D , we minimize the lowest singular value S_{\min} of the matrix in Eq. (5) to identify the eigenmodes of the system. The metric of the S_{\min} is advantageous over that of the determinant (see Sec. 6 in Supplementary Material [24] for more details).

ACKNOWLEDGMENTS

X.W. and C.R. acknowledge support by the Helmholtz Association via the Helmholtz program ‘‘Materials Systems Engineering’’ (MSE). P.G., A.G.L., and C.R. are part of the Max Planck School of Photonics, supported by the Bundesministerium f ur Bildung und Forschung, the Max Planck Society, and the Fraunhofer Society. P.G. acknowledges support from the Karlsruhe School of Optics and Photonics (KSOP). P.G. and C.R. acknowledge support by the German Research Foundation within the SFB 1173 (Project-ID No. 258734477). The authors would like to thank Prof. Sergei Tretyakov for the fruitful discussions on the application of the designed photonic time crystals for constructing a perfect lens.

* These authors contributed equally.

- [1] E. Galiffi, R. Tirole, S. Yin, H. Li, S. Vezzoli, P. A. Huidobro, M. G. Silveirinha, R. Sapienza, A. Al , and J. Pendry, *Advanced Photonics* **4**, 014002 (2022).
- [2] N. Engheta, *Nanophotonics* **10**, 639 (2020).
- [3] J. R. Zurita-S anchez, P. Halevi, and J. C. Cervantes-Gonz alez, *Physical Review A* **79**, 053821 (2009).
- [4] E. Lustig, Y. Sharabi, and M. Segev, *Optica* **5**, 1390 (2018).
- [5] M. Lyubarov, Y. Lumer, A. Dikopoltsev, E. Lustig, Y. Sharabi, and M. Segev, *Science* **377**, 425 (2022).
- [6] A. Dikopoltsev, Y. Sharabi, M. Lyubarov, Y. Lumer, S. Tsesses, E. Lustig, I. Kaminer, and M. Segev, *Proceedings of the National Academy of Sciences* **119**, e2119705119 (2022).
- [7] Y. Pan, M.-I. Cohen, and M. Segev, *Physical Review Letters* **130**, 233801 (2023).
- [8] Z. Hayran, J. B. Khurgin, and F. Monticone, *Optical Materials Express* **12**, 3904 (2022).
- [9] J. Reyes-Ayona and P. Halevi, *Applied Physics Letters* **107** (2015).
- [10] J. Park, H. Cho, S. Lee, K. Lee, K. Lee, H. C. Park, J.-W. Ryu, N. Park, S. Jeon, and B. Min, *Science advances* **8**, eabo6220 (2022).
- [11] X. Wang, M. S. Mirmoosa, V. S. Asadchy, C. Rockstuhl, S. Fan, and S. A. Tretyakov, *Science Advances* **9**, eadg7541 (2023).
- [12] I. A. Williamson, M. Minkov, A. Dutt, J. Wang, A. Y. Song, and S. Fan, *Proceedings of the IEEE* **108**, 1759 (2020).
- [13] B. Borchers, C. Br ee, S. Birkholz, A. Demircan, and G. Steinmeyer, *Optics letters* **37**, 1541 (2012).
- [14] M. Z. Alam, I. De Leon, and R. W. Boyd, *Science* **352**, 795 (2016).
- [15] J. Bohn, T. S. Luk, S. Horsley, and E. Hendry, *Optica* **8**, 1532 (2021).
- [16] Y. Zhou, M. Z. Alam, M. Karimi, J. Upham, O. Reshef, C. Liu, A. E. Willner, and R. W. Boyd, *Nature communications* **11**, 2180 (2020).
- [17] L. Caspani, R. Kaipurath, M. Clerici, M. Ferrera, T. Roger, J. Kim, N. Kinsey, M. Pietrzyk, A. Di Falco, V. M. Shalaev, *et al.*, *Physical review letters* **116**, 233901 (2016).
- [18] J. B. Khurgin, M. Clerici, and N. Kinsey, *Laser & Photonics Reviews* **15**, 2000291 (2021).
- [19] E. Lustig, O. Segal, S. Saha, E. Bordo, S. N. Chowdhury, Y. Sharabi, A. Fleischer, A. Boltasseva, O. Cohen, V. M. Shalaev, *et al.*, *Nanophotonics* (2023).
- [20] J. B. Khurgin, arXiv preprint arXiv:2305.15243 (2023).
- [21] J. B. Khurgin, ‘‘Energy and Power requirements for alteration of the refractive index,’’ (2023), arxiv:2308.16011 [physics].
- [22] M. Mirmoosa, T. Koutserimpas, G. Ptitsyn, S. Tretyakov, and R. Fleury, *New Journal of Physics* **24**, 063004 (2022).
- [23] V. Asadchy, A. Lamprianidis, G. Ptitsyn, M. Albooyeh, T. Karamanos, R. Alaee, S. Tretyakov, C. Rockstuhl, S. Fan, *et al.*, *Physical Review Applied* **18**, 054065 (2022).
- [24] See Supplemental Material for additional information.
- [25] J. C. Serra and M. G. Silveirinha, ‘‘Homogenization of dispersive spacetime crystals: Anomalous dispersion and negative stored energy,’’ (2023), arXiv:2306.11194 [physics.optics].
- [26] D. Sievenpiper, L. Zhang, R. F. Broas, N. G. Alexopolous, and E. Yablonovitch, *IEEE Transactions on Microwave Theory and techniques* **47**, 2059 (1999).
- [27] S. Tretyakov, *Analytical modeling in applied electromagnetics* (Artech House, 2003).
- [28] D. M. Pozar, *Microwave engineering* (John Wiley & sons, 2011).
- [29] J. B. Pendry, *Physical review letters* **85**, 3966 (2000).
- [30] A. Rahimzadegan, R. Alaee, C. Rockstuhl, and R. W. Boyd, *Opt. Express* **28**, 16511 (2020).
- [31] P. Garg, A. G. Lamprianidis, D. Beutel, T. Karamanos, B. Verf urth, and C. Rockstuhl, *Opt. Express* **30**, 45832 (2022).
- [32] R. Venkitakrishnan, T. H ob, T. Rep an, F. Z. Goffi, M. Plum, and C. Rockstuhl, *Phys. Rev. B* **103**, 195425 (2021).
- [33] J. D. Joannopoulos, S. G. Johnson, J. N. Winn, and R. D. Meade, *Photonic Crystals: Molding the Flow of Light (Second Edition)*, 2nd ed. (Princeton University Press, 2008).
- [34] S. Fan and J. D. Joannopoulos, *Phys. Rev. B* **65**, 235112 (2002).